Journal of *Marine Science and Engineering*

MDPI

Article

Development and Testing of an In Situ Observation Device for Seafloor Boreholes

Haodong Deng [1,3], Jianping Zhou [2,3,*], Xiaotao Gai [1,*], Chunhui Tao [3] and Bin Sui [4]

[1] School of Marine Engineering Equipment, Zhejiang Ocean University, Zhoushan 316000, China; denghaodong77@163.com
[2] State Key Laboratory of Submarine Geoscience, Ministry of Natural Resources, Hangzhou 310012, China
[3] Second Institute of Oceanography, Ministry of Natural Resources, Hangzhou 310027, China; taochunhuimail@163.com
[4] Hangzhou Hanlu Geophysical Exploration Co., Ltd., Hangzhou 310027, China; suibin95@163.com
* Correspondence: zhoujp@sio.org.cn (J.Z.); gaixt@zjou.edu.cn (X.G.)

Abstract

Seafloor hydrothermal systems at mid-ocean ridges are focal points for heat and matter exchange between the seawater and lithosphere. While seafloor seismographs (OBS) and pressure recorders (BPR) are standard for regional monitoring, achieving high-precision, vertical sub-surface data in complex hydrothermal terrains remains a significant technical objective. This study presents a novel in situ penetration probe designed for multi-parameter monitoring of marine hydrothermal vent areas. A key innovation of this work is its operational versatility and engineering efficiency: the probe is specifically designed for post-drilling deployment in boreholes, effectively utilizing existing coring sites to achieve direct coupling with the deep-seated crust, or for targeted placement via Remotely Operated Vehicles (ROVs). The device integrates a titanium-alloy conical tip and cylindrical chamber, housing tri-axial accelerometers and dual temperature-pressure sensors. Numerical simulations using the SST k-ω turbulence model and finite element analysis optimized the cone aperture and assessed fluid–structure stability under deep-sea conditions. Laboratory vibration tests and shallow-water sea trials validated the probe's basic dynamic response, electromechanical integrity, and capability to acquire coupled environmental parameters. This compact, modular design provides a scalable and cost-effective framework for precise three-dimensional observation of sub-surface hydrothermal processes and deep-sea resource exploration.

Keywords: hydrothermal fluid; in situ probe; seafloor observation; CFD simulation

Check for updates

Academic Editor: Weicheng Cui

Received: 10 March 2026
Revised: 30 March 2026
Accepted: 1 April 2026
Published: 22 April 2026

Copyright: © 2026 by the authors. Licensee MDPI, Basel, Switzerland. This article is an open access article distributed under the terms and conditions of the Creative Commons Attribution (CC BY) license.

1. Introduction

Modern seafloor hydrothermal activity at mid-ocean ridges is a crucial process driving the exchange of heat and matter between seawater and the lithosphere [1]. Driven by hydrothermal mineralization at mid-ocean ridges, large quantities of metal sulfides precipitate from hydrothermal fluids to form sulfide deposits [2]. Consequently, marine resources such as seafloor polymetallic sulfide deposits have increasingly become the focus of international attention and may trigger deep-sea mining in the next decade [3–5]. The exploration of these deposits helps relieve pressure on terrestrial resources and promotes the development of deep-sea exploration and mining technologies, facilitating the sustainable utilization of marine resources.

In situ observation of seafloor hydrothermal activity centers on monitoring dynamic vibrations within hydrothermal regions, alongside pressure and temperature trends driven by hydrothermal cycling [6]. By leveraging observational data, researchers can extract critical information about the structural composition of the seafloor and elucidate the metallogenic mechanisms governing these hydrothermal zones. Over the past few decades, various observation methodologies have been developed. For instance, the National Oceanic and Atmospheric Administration (NOAA) established the New Millennium Observatory Network (NeMO) [7], which integrates Ocean Bottom Seismometers (OBS), Bottom Pressure Recorders (BPR), and other sensors to study volcanic perturbations [8]. Another pioneering approach is deep-sea drilling observation [9], such as the MeBoCORK system deployed in the Nankai Trough, which places sensors within deep-sea boreholes for long-term monitoring [10–12]. To systematically evaluate the capabilities of these existing technologies, a performance benchmarking of representative in situ observation systems is summarized in Table 1.

Table 1. Performance benchmarking of state-of-the-art deep-sea in situ observation systems.

System/Technology	Deployment Method	Key Measured Parameters	Observation Zone
NeMO Network	Seafloor observatory nodes	Seismic, acoustic, pressure, geochemical	Seafloor surface
Traditional OBS	Pop-up deployable nodes	Micro-seismic	Seafloor surface
MeBoCORK	Downhole drilling rig	Temperature, pressure	Deep boreholes
Proposed Probe	Direct borehole insertion	Temperature, pressure, seismic (MEMS)	Sulfide deposit boreholes

As summarized in Table 1, existing systems have significantly advanced ocean exploration. Currently, pop-up ocean bottom seismometers (OBS) offer an efficient method for large-scale surface monitoring. However, relying solely on surface sensors inherently restricts the capability to conduct high-resolution, three-dimensional observations of the shallow sub-surface regions within polymetallic sulfide deposits. To access these critical sub-surface zones, downhole stations (e.g., MeBoCORK) are frequently utilized; yet, their instrumentation is often sparse, typically providing only basic temperature and pressure data without the integration of high-frequency seismic monitoring. Conversely, specialized downhole seismometers focus exclusively on seismic detection, lacking comprehensive multi-parameter (temperature and pressure) data acquisition capabilities. To overcome these limitations, there is an urgent need to develop a highly integrated, multi-parameter observation probe specifically tailored for the dynamic and confined environments of 4000 m deep seafloor hydrothermal boreholes.

To overcome these limitations, there is an urgent need for a highly integrated, multi-parameter observation probe specifically designed for the dynamic and constrained environment of subsea hydrothermal boreholes. Therefore, this study proposes a novel compact in situ observation probe designed for direct deployment within sulfide deposit boreholes. Specifically, the probe is engineered to strategically utilize the residual boreholes left behind after core sampling operations by seafloor drills, thereby maximizing the scientific utility of existing drill sites. Furthermore, its highly integrated form factor allows for flexible, precision deployment by Remotely Operated Vehicles (ROVs). To ensure high-fidelity data acquisition in extreme environments, the system was developed following specific performance objectives and design specifications: (1) strict borehole deployment size limitations, requiring an instrument outer diameter not exceeding 65 mm, necessitating the integration of miniaturized, low-power MEMS sensors for triaxial dynamic vibration monitoring;

(2) long-term, high-precision thermodynamic observation capabilities, specifically targeting a temperature measurement range of 273.15–363.15 K and a pressure measurement range of 0–45 MPa with an accuracy of ±0.05% FS (Full Scale); (3) enhanced coupling with sulfide sediments while protecting the bottom sensor through an optimized 2.0 mm micro-hole array design. This system aims to provide reliable, high-resolution coupled data for deep-sea hydrothermal exploration.

Herein, a novel in situ observation probe for submarine hydrothermal environments is proposed. This design addresses the limitations of large volume and surface-only observation associated with traditional observation stations, chains, and nets, while also overcoming the sparse instrumentation common in drilling-based systems. The remainder of this paper is organized as follows. Section 2 details the in situ observation probe, including its structural and circuit design. Section 3 describes the numerical analysis of the probe. Section 4 describes laboratory vibration tests and shallow-sea trials. Section 5 discusses the experimental results. Finally, Section 6 presents the study's conclusions.

2. Design of the In Situ Observation Rod Device

In 2011, China secured a 10,000 km^2 exploration contract area for polymetallic sulfides on the Southwest Indian Ridge (SWIR), granting priority mining rights. Recent investigations into the metallogenic models of ultraslow-spreading ridges and specific case studies of the Duanqiao field have revealed complex sub-seafloor hydrothermal processes that require precise in situ observation [13,14]. Observation of these geological features allows for the inference of the deposit's structural characteristics, providing valuable data to support mineral resource exploration and development in this region.

As depicted in Figure 1, the observation probe is designed for sub-surface insertion into these polymetallic sulfide formations, deployed via a drilling system or a remotely operated vehicle (ROV). This deployment method stands in sharp contrast to traditional, surface-based observation networks. By positioning the probe within the seabed and thus closer to the seismic source, the signal attenuation caused by wave propagation through the water column is significantly reduced. This results in higher-fidelity data and enables stable, long-term monitoring.

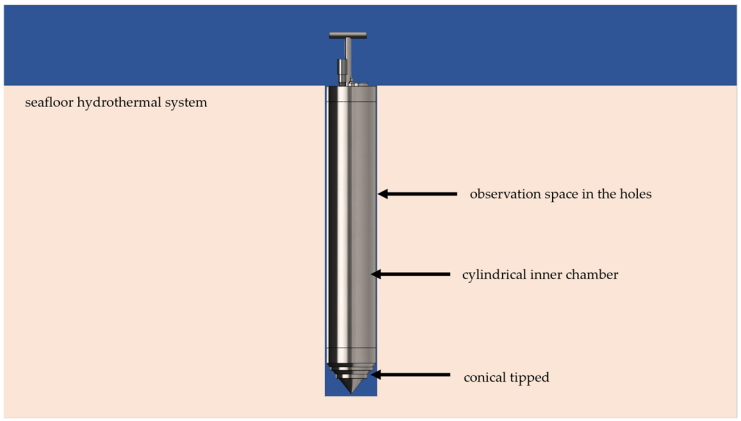

Figure 1. Schematic diagram of in situ observation probe deployment.

Furthermore, temperature and pressure sensors integrated at both ends of the probe enhance its vertical spatial resolution. This dual-sensor configuration allows for the precise quantification of sub-surface thermal and pressure gradients. This design improves overall measurement accuracy and provides a more comprehensive understanding of the dynamic processes occurring within the deposit formation.

2.1. Structural Design

Figure 2 shows a three-dimensional model of the observation probe. In consideration of the complex topography of polymetallic sulfide deposits, the titanium-alloy housing is designed with a cylindrical inner chamber and a conical-tipped base. This conical structure facilitates penetration into the seabed deposit and ensures robust coupling with the sediment. comprises three accelerometers. To capture high-fidelity vibration data, a high-precision microelectromechanical system SIA202 (Manufactured by Qingdao ZITN Microelectronics Co., Ltd., Qingdao, China) triaxial accelerometer was employed as the primary sensor. While traditional piezoelectric seismometers and moving-coil geophones offer excellent sensitivity, their bulky form factors and high power consumption render them unsuitable for highly constrained deep-sea environments. In contrast, MEMS technology provides a remarkably compact footprint. The specific performance parameters of the chosen MEMS accelerometer are summarized in Table 2.

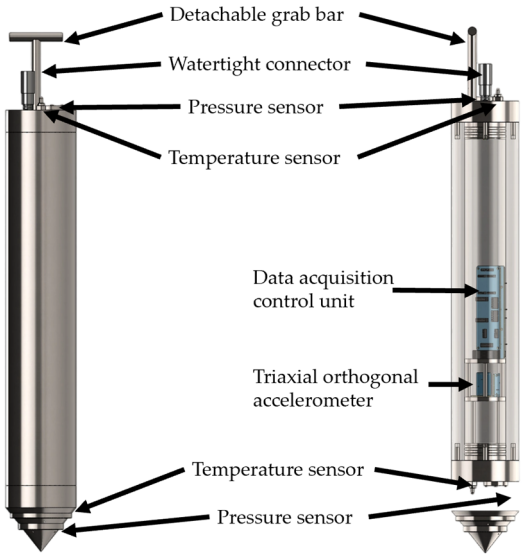

Figure 2. The in situ observation probe.

Table 2. Accelerometer performance parameters.

Parameter	Unit	Specification
Measurement Range	g	±2
Bias	mg	0.14
Bias Stability	μg	3
Power consumption	mW	10
Noise Threshold (1 Hz)	μg rms	7
Operating temperature	K	233.15–398.15

The cone itself is a hollow structure with open apertures. This allows bottom-mounted sensors to accurately measure the external environment, but it also introduces structural integrity challenges under immense deep-sea pressure. To overcome potential stress concentrations, structural stiffeners are added to the cone's surface to enhance its stability. Furthermore, the cylindrical titanium chamber is fitted with a gradient (i.e., the difference) in pressure and temperature between the seafloor surface and the target depth within the deposit. The cylindrical chamber also houses the accelerometer and core control circuitry.

Seismic signals from the hydrothermal deposit are transmitted directly through the probe's housing to the internal accelerometer. This sub-surface coupling mechanism is fundamentally different from surface-based OBS observations [15]. By bypassing the water

column, signal attenuation during propagation is significantly reduced, which improves signal quality, yields higher resolution, and provides superior noise rejection [16].

2.2. Circuit Design

The data acquisition system (DAS) of the in situ observation probe comprises three accelerometers, two pressure sensors, and two temperature sensors. All sensors employ a MEMS architecture. Due to their compact size, low power consumption, and immunity to electromagnetic interference, high-performance MEMS sensors are increasingly replacing conventional geophones in modern geophysical exploration [17]. To ensure comprehensive 3D motion sensing, the three accelerometers are orthogonally mounted along the X, Y, and Z axes. The pressure and temperature sensors are placed at the top and bottom of the cylindrical housing to measure vertical gradients. Figure 3 presents the circuit system block diagram for the DAS [18].

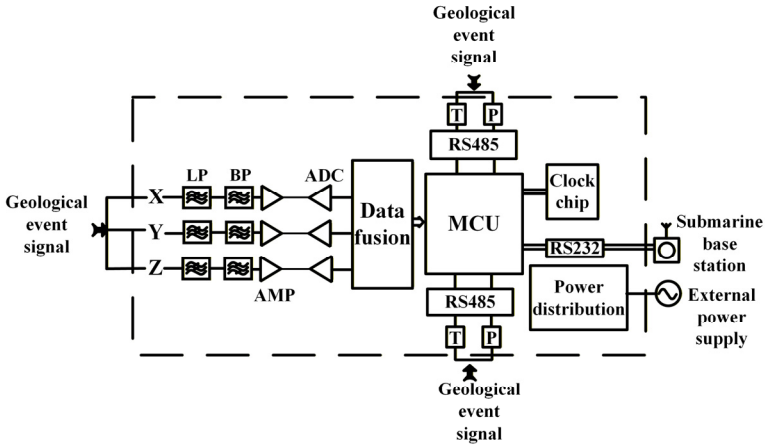

Figure 3. The circuit system block diagram.

The signal path for the X, Y, and Z accelerometers undergoes a filtering stage followed by differential amplification before being digitized by the Analog-to-Digital Converter (ADC). In contrast, signals from the pressure and temperature sensors are at both the top and bottom ends. This configuration is designed to record the vertical temperature sensors that are converted directly by a separate ADC and transmitted as digital signals to the Microcontroller Unit (MCU). External peripherals for the MCU include an RS485 circuit, an RS232 interface, a USB interface, and a high-precision clock chip.

The power supply system for the DAS receives a 12 V external input and uses a step-down voltage regulator to supply the operating power for the accelerometers, pressure and temperature sensors, and the MCU. All system power, data transmission, and communication are handled via an RS232 interface, which connects to an external submarine base station through a watertight connector at the top of the in situ observation probe.

3. Numerical Analysis

3.1. Observation Rod Model

As illustrated in Figure 4, the penetration cone at the base of the observation probe is constructed from a titanium alloy. This specially engineered component serves three critical functions: (1) facilitating fluid exchange to ensure the embedded temperature and pressure sensors are responsive to the surrounding marine sediments; (2) providing robust geotechnical protection for the sensor arrays against sub-surface stresses via its tapered geometry; and (3) ensuring structural continuity with the main probe body, achieved by matching the outer diameter.

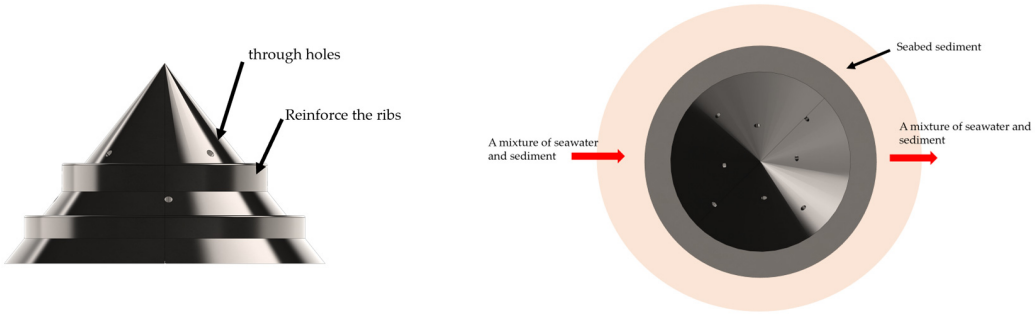

(**a**) (**b**)

Figure 4. The penetration cone structure: (**a**) overall model of the bottom cone tip; (**b**) the fluid-solid coupling process between the bottom cone tip and seabed sediments.

The conical design incorporates three key engineering optimizations: (1) strategically positioned reinforcing ribs (stiffeners) enhance structural integrity, ensuring stability during penetration in high-pressure deep-sea environments; (2) precision-machined apertures (through-holes) that enable controlled fluid exchange [19], allowing internal sensors to measure external conditions; and (3) a hydrodynamically optimized tip geometry that facilitates efficient penetration into seabed sediments while minimizing substrate disturbance.

3.2. Simulation Method

The sensor performance is critically dependent on the aperture size, necessitating a balance among three key functional trade-offs. First, while a larger aperture enhances inflow velocity and accelerates sensor response time, it also intensifies turbulence, which can introduce measurement deviations. Second, structural analysis reveals a critical aperture threshold; exceeding this limit induces excessive material stress and can lead to critical stress concentrations. Third, a larger orifice nonlinearly increases the risk of sediment intrusion and potential clogging.

To identify the optimal design and evaluate the balance between fluid exchange efficiency and internal stability, a comprehensive three-dimensional Computational Fluid Dynamics (CFD) model was established using Ansys Fluent (Version 2024 R2). Similar CFD-based optimization strategies have been successfully applied to the design of deep-sea samplers to minimize disturbance [20]. The numerical model is physically composed of three interactive components: an external fluid domain simulating the surrounding deep-sea environment, an internal fluid domain representing the sensor cavity, and a solid domain for the TC4 titanium alloy probe structure. To accurately capture the hydrodynamic performance and thermal-fluid-solid coupling effects, the computational domain was discretized utilizing a Watertight Geometry workflow. This advanced approach ensures perfect topological continuity between the external deep-sea environment and the internal chamber, completely eliminating artificial boundary barriers.

A high-quality polyhedral mesh strategy was employed. Polyhedral elements were chosen over traditional tetrahedral elements as they significantly reduce numerical diffusion and lower the total element count while maintaining high computational accuracy. Instead of relying on a traditional posteriori grid independence study, the mesh resolution was strictly determined a priori based on the physical scales of the micro-apertures to eliminate numerical dissipation. While the global maximum cell length was set to approximately 9.5 mm, a local proximity face sizing of 0.2 mm was strictly enforced at the 2.0 mm structural apertures. This specific sizing ensures that at least 10 computational cells span the diameter of each aperture, strictly satisfying the fundamental CFD requirement for capturing micro-scale jet flows and shear layers. Furthermore, three layers of prism elements with a smooth transition ratio of 1.2 were generated on the fluid-solid interfaces. Consequently, the high-

fidelity mesh comprising a total of 8,678,488 polyhedral and prism elements was finalized, yielding an excellent minimum orthogonal quality of 0.15. The final mesh configuration and the local refinement details are illustrated in Figure 5.

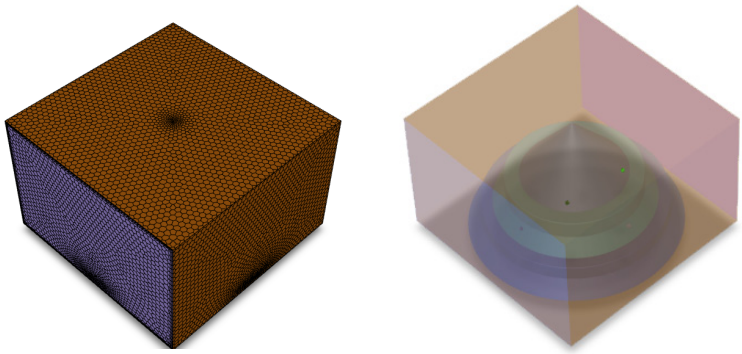

(**a**) (**b**)

Figure 5. Meshing diagram of the simulation model: (**a**) meshing diagram; (**b**) grid perspective view with the bottom cone tip surrounded by seafloor sediments.

The simulation was conducted under steady-state conditions using the pressure-based Coupled algorithm, which provides superior robust convergence for complex polyhedral meshes. The Shear-Stress Transport (SST) k-ω turbulence model was employed, as it is highly reliable for predicting flow separation and adverse pressure gradients around complex conical geometries. Crucially, the Energy equation was enabled to solve for the coupled fluid flow and heat transfer across the hollow conical structure with the specified thermal conductivity of the titanium alloy. The working fluid was defined as liquid water with a constant density of 1024 kg/m^3 to simulate the deep-sea environment. The inlet boundary was set as a velocity inlet with a typical deep-sea bottom current speed of 0.05 m/s, while the outlet was defined as a pressure outlet (0 Pa gauge pressure). During the computational process, strict convergence criteria were enforced. The solution was considered fully converged when the scaled residuals of the continuity, momentum, energy, and specific dissipation rate equations dropped below 10^{-4}, and the monitored physical quantities reached a stable horizontal asymptote. Driven by the high-quality mesh and the robust Coupled solver, the numerical solution demonstrated excellent stability and achieved strict convergence in exactly 46 iterations.

The simulation was conducted under steady-state conditions. To maximize the efficiency and stability of the 8.68 million polyhedral mesh, the pressure-based Coupled algorithm was employed for pressure-velocity coupling, superseding traditional segregated algorithms. Furthermore, second-order upwind schemes were utilized for spatial discretization to ensure high numerical accuracy. The Shear-Stress Transport (SST) k-ω [21] turbulence model was specifically selected because it accurately simulates both far-field turbulent flow (critical for interacting with seabed sediments) and complex near-wall boundary layer physics under the pressure gradients of the deep-sea environment. Crucially, the Energy equation was enabled to simultaneously solve for the coupled fluid flow and heat transfer across the solid titanium alloy structure [22].

The computational domain effectively consists of two fluid domains and one solid domain. For the external fluid domain, the upstream boundary was defined as a velocity inlet with a typical deep-sea bottom current speed of 0.05 m/s, while the opposite boundary was designated as a pressure outlet (0 Pa gauge pressure). The remaining far-field boundaries were set as walls. The working fluid was defined as liquid water with a constant density of 1024 kg/m^3 to replicate the deep-sea environment.

During the computational process, rigorous convergence criteria were enforced. The convergence characteristics were monitored by tracking the scaled residuals of the continuity, momentum, energy, and specific dissipation rate equations. Furthermore, a specific monitor point was strategically placed within the cone's interior chamber to continuously track temperature and pressure variations. The steady-state solution was considered fully converged only when all respective residuals dropped below 10^{-4} and the physical quantities at the internal monitor point reached a stable horizontal asymptote. Driven by the high-quality polyhedral mesh [23] and the robust Coupled solver, the numerical solution demonstrated exceptional stability and achieved strict convergence in exactly 46 iterations.

As shown in Table 3 below, the temperature and pressure field distribution under different apertures verified the stability advantage of this critical size.

Table 3. Comparison of simulation structures with different apertures under the same configuration.

	Working Condition 1	Working Condition 2	Working Condition 3
Aperture size (mm)	1.0	1.5	2.0
Temperature field (K)	269.90	269.57	271.6174
Pressure field (ΔP)	0.5	0.2	0.0

4. Experiments

The seabed in situ observation probe and its associated sampling circuitry were fully realized, and the assembled system is illustrated in Figure 6. The data acquisition system is engineered for multi-parameter monitoring and features a modular design with a clear physical separation between the sensing modules and the main control electronics.

(**a**) (**b**)

Figure 6. Submarine in situ probe and its supporting sampling circuit: (**a**) temperature and pressure acquisition board in the circuit system; (**b**) MCU peripheral circuits and ADC circuits in the circuit system.

As shown in Figure 6a, a dedicated acquisition board manages the low-speed environmental sensors. It is engineered to collect data from four channels (two temperature and two pressure sensors). These sensors communicate with the MCU via the RS485 protocol, which was selected for its robust, noise-resistant data transmission capabilities over the required subsea distances.

Figure 6b presents the core control board, which serves as the probe's central electronic platform. This board integrates the MCU, the power management unit, the RS232 commu-

nication interface, and the ADC modules required for processing the high-rate acceleration data. A tri-axial accelerometer was affixed near the lower end cap of the titanium housing. The sensor's axes were precisely aligned with the probe's three orthogonal axes, and its position was adjusted to minimize the gap between the accelerometer and the end cap. This mounting configuration ensures high-fidelity mechanical coupling and enhances structural stiffness, thereby guaranteeing accurate dynamic response measurements [24].

In operation, the MCU orchestrates the timing and coordination of all acquisition tasks. The ADC module performs high-rate, synchronized sampling of the three-axis acceleration signals, while the RS485 interface concurrently collects the low-speed temperature and pressure data. Through this integrated architecture, the probe achieves simultaneous monitoring of both static and dynamic environmental parameters, providing a comprehensive dataset for in situ seabed observations.

4.1. Accelerometer Test

Figure 7 illustrates the experimental setup of the vibration table test (WN-Z023), which was conducted to evaluate the dynamic response characteristics of the observation probe under controlled harmonic excitation. To ensure stable mechanical coupling and to avoid relative motion during vibration loading, the tip section of the probe was detached and rigidly fixed to the surface of the shaker. Sinusoidal excitations at 3 Hz, 10 Hz, and 20 Hz were sequentially applied along the three orthogonal axes (X, Y, and Z). These frequencies were selected to cover the representative low-frequency operating range of the probe and to characterize its response under weak, moderate, and relatively stronger dynamic excitation conditions. Specifically, 3 Hz was used to represent very low-frequency vibration, 10 Hz to characterize the intermediate response behavior, and 20 Hz to evaluate the upper limit of the low-frequency response band, where dynamic amplification and directional sensitivity could be more clearly identified.

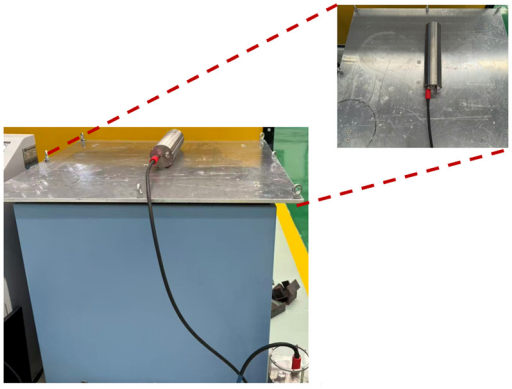

Figure 7. Vibration table testing.

Acceleration signals were acquired using the probe's internally integrated tri-axial accelerometer. For each excitation condition, data were sampled at 200 Hz for 60 s. During post-processing, the recorded data were first screened to retain steady-state segments and to exclude abnormal portions associated with unstable amplitude or spectral deviation. The selected acceleration signals were then processed using a polynomial least-squares fitting method, in which a low-order polynomial trend was fitted to the time-domain signal and subsequently removed to suppress slow-varying baseline components and non-stationary drift while preserving the main vibration response. After filtering, Fast Fourier Transform (FFT) analysis was performed to identify the dominant frequency components of the probe response. In parallel, Power Spectral Density (PSD) was estimated using Welch's method with a Hann window and 50% overlap to obtain a statistically stable

description of spectral energy distribution. By comparing the spectral peaks and energy distributions under different excitation frequencies and loading directions, the frequency-response characteristics, directional sensitivity, and cross-axis coupling behavior of the observation probe were systematically evaluated [25].

4.2. Sea Trial

The operational capability of the subsea in situ probe system was verified through a shallow-water sea trial conducted in the waters off Laoshan, Qingdao. The deployment setup is illustrated in Figure 8. The probe system, designed for long-term seabed monitoring, consists of two main parts: the heavy deployment base (yellow housing) and the seabed in situ observation probe (thumbnail in the upper right corner). The probe's deployment base (seabed machine) is being carefully lowered into the water by a shipborne crane.

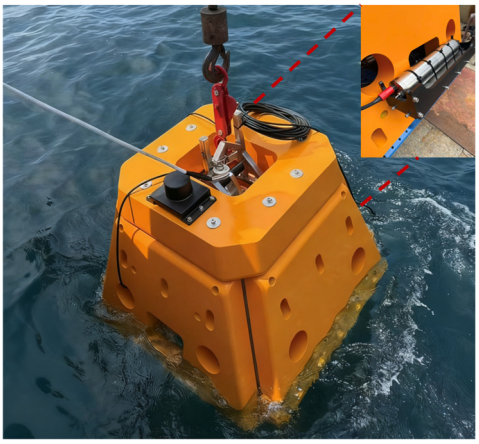

Figure 8. Deploy the seabed machine in the shallow sea experiment.

The deployment sequence begins with the seabed machine (deployment base) being hoisted from the ship's deck by a winch. The observation probe is suspended from this base by a cable. Once the seabed machine is positioned just above the seafloor, the cable is "paid out" (i.e., released), allowing the probe to free-fall and penetrate the seabed sediment. Subsequently, the probe remains connected to the seabed machine via this tether to enable power and data transmission. The water depth at this trial location was approximately 20 m.

5. Results and Discussion

5.1. Shallow Experimental Data

Figure 9 presents both the time-domain waveforms and the corresponding frequency-domain (Welch PSD) analysis of the acceleration data. To comprehensively evaluate the probe's dynamic response and frequency generalization capability across different regimes, a three-tier frequency testing strategy was adopted. The shaker tests were conducted at targeted excitation frequencies of (a) 3 Hz, (b) 10 Hz, and (c) 20 Hz. This specific combination was strategically selected based on the following rationale: 3 Hz (low-frequency band) directly addresses the typical frequency range of natural seabed hydrothermal activity (which is generally below 6–8 Hz), effectively reflecting the impact of micro-seismic or slowly varying disturbances on the waveform baseline and spectral noise floor; 10 Hz (mid-frequency band) serves as a transitional condition between the low and high-frequency regimes, utilized to verify the cross-band consistency and stability of the measurement model; and 20 Hz (high-frequency band) represents a higher operating frequency and a standard calibration condition for fixed-frequency shaker table tests, facilitating comparisons with

established experimental protocols. This combination successfully covers the low, mid, and high-frequency response spectrums without increasing experimental complexity.

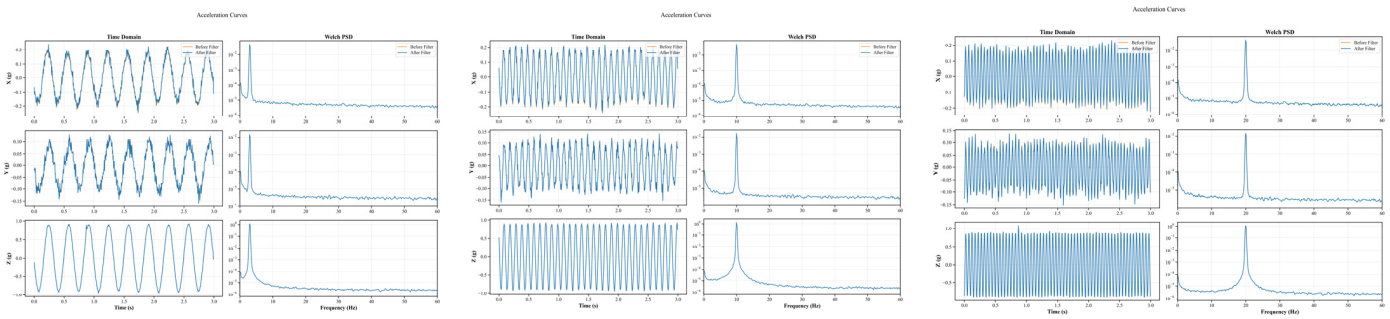

(**a**) (**b**) (**c**)

Figure 9. Time-domain acceleration waveforms and corresponding Welch PSD frequency-domain responses under different excitation frequencies: (**a**) 3 Hz; (**b**) 10 Hz; (**c**) 20 Hz.

In the time-domain plots (left column of each subfigure), the raw ("Before Filter") and processed ("After Filter") signals are compared. The applied filtering process effectively preserves the amplitude and phase integrity of the target signals without introducing distortion.

The frequency-domain plots (right column) further confirm the system's performance. The Welch PSD analysis reveals sharp, dominant magnitude peaks precisely at the target excitation frequencies (3 Hz, 10 Hz, and 20 Hz). Concurrently, the background noise floor across other frequency bands is substantially suppressed. Crucially, these clear response peaks and high signal-to-noise ratios are consistent across all three orthogonal axes (X, Y, and Z) for every test condition, demonstrating the probe's robust multi-axis sensitivity and reliable dynamic response from low to higher frequency bands.

Figures 10a and 10b present the abnormal vibration events recorded by the tri-axial accelerometer during the deployment (10:00–10:30) and retrieval (16:00–16:30) phases, respectively. The data has been band-pass filtered between 1.0 Hz and 3.0 Hz to isolate these low-frequency dynamic events.

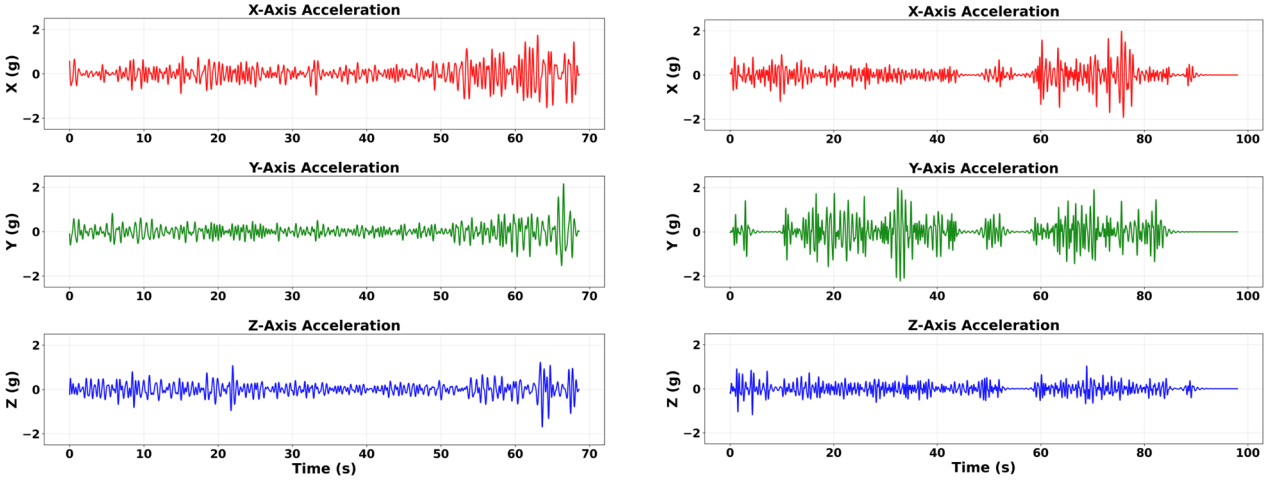

(**a**) (**b**)

Figure 10. Acceleration waveform plot: (**a**) abnormal vibration events recorded by the three-axis accelerometer during the deployment process from 10:00 to 10:30; (**b**) abnormal vibration events recorded by the three-axis accelerometer during the recovery process from 16:00 to 16:30.

The analysis reveals that both operational phases are characterized by significant transient vibration events rather than sustained oscillations. A visual comparison confirms

that the retrieval phase (Figure 10b) induced a substantially more intense vibration response than the deployment phase (Figure 10a). This is particularly evident in the large burst of activity after the 55 s mark in Figure 10b.

Notably, these high-amplitude events during retrieval are concentrated in the horizontal plane (X and Y axes), with peak amplitudes approaching ±2 g (see Y-axis, Figure 10b). This response pattern strongly suggests a significant pendulum motion of the probe as it was being lifted through the water column, contrasting sharply with the comparatively moderate vertical (Z-axis) oscillations. This finding is critical for assessing the mechanical stresses the probe must endure during operational maneuvers.

Figure 11 presents the time-series data from the dual temperature and pressure sensors recorded during the sea trial's retrieval phase.

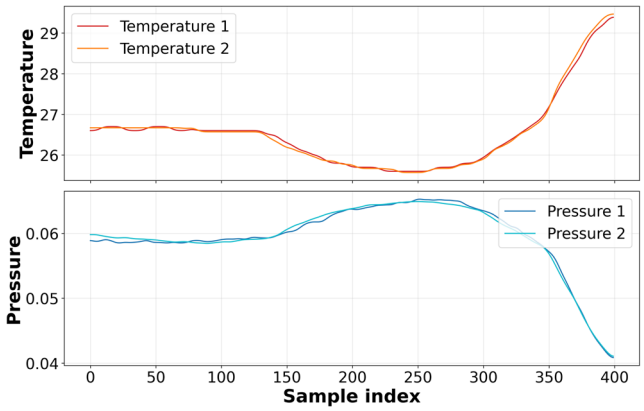

Figure 11. Temperature and pressure waveform plot.

The temperature analysis (top plot) demonstrates a high degree of correlation between Sensor 1 (top cap) and Sensor 2 (bottom cap), with a maximum deviation of less than 0.2 °C. This validates the sensor pair's high-fidelity tracking of the external environment. A distinct thermal gradient is evident in the final stage of the recording, where the temperature rises sharply from ~25.7 °C to over 29 °C. This clearly captures the probe's ascent through the thermocline into the warmer, near-surface water layer.

The pressure analysis (bottom plot) also shows a strong correlation between the two sensors. The data captures the dynamic pressure change as the probe is lifted, rising slightly before dropping sharply as the probe surfaces. This dynamic signal confirms the pressure system's responsiveness to changes in depth during retrieval.

5.2. Discussion

The structural design of the probe's conical tip, initially discussed in Section 3, fundamentally aims to optimize the physical coupling between the internal sensors and the complex fluid environment. Since the probe is primarily deployed inside drilled boreholes within seafloor sulfide deposits, it is imperative that the device accurately measures the confined borehole fluid and pore water without any structural signal distortion. To systematically evaluate this, a parametric study was conducted to analyze the effect of varying the aperture size (1.0 mm, 1.5 mm, and 2.0 mm) on measurement accuracy. As the aperture diameter increases to 2.0 mm, the internal flow resistance is significantly minimized, effectively equalizing the internal and external pressure fields. This eliminates pressure signal attenuation and ensures the internal sensor captures the true hydrostatic and hydrodynamic pressure within the borehole. Concurrently, for temperature detection, the enhanced fluid exchange efficiency mitigates the thermal interference caused by internal electronic heating. The optimal 2.0 mm aperture facilitates sufficient cold borehole fluid intrusion to suppress the localized temperature rise, preventing artificial thermal

accumulation from polluting the environmental temperature signal. Consequently, the 2.0 mm aperture was selected as the optimal structure to maximize both temperature and pressure detection accuracy in the confined borehole environment.

To further elucidate the physical mechanism behind this enhanced sensing accuracy, the internal hydrodynamic and thermal fields for the optimal 2.0 mm configuration are visualized. As illustrated by the cross-sectional velocity contour (Figure 12c,d), while the external fluid flows past the probe at 0.05 m/s (simulating the bottom current or borehole seepage), the micro-apertures act as an effective hydrodynamic damper. The internal chamber velocity is drastically reduced to a near-stagnant state (<0.01 m/s), providing a stable, low-noise microenvironment that prevents dynamic flow fluctuations from interfering with the sensitive static sensor readings. Furthermore, the static pressure distribution (Figure 12a) reveals a completely unimpeded pressure transmission between the internal cavity and the external borehole environment, confirming that the protective housing induces no artificial pressure bias. Crucially, the thermal-fluid-solid coupling temperature contour (Figure 12b) explicitly demonstrates the mechanism for ensuring thermal detection accuracy. The continuous influx of cold deep-sea fluid (271.15 K) rapidly neutralizes the heat generated by the internal electronics. While the inner wall maintains a slight temperature gradient (peaking at 274.93 K), the central sensing region is effectively cooled by the convective cold water tongue. This strong thermal-fluid coupling ensures that the temperature sensor is predominantly exposed to the authentic properties of the external sulfide borehole fluid rather than the self-heating of the titanium housing, thereby guaranteeing the ultimate accuracy and reliability of the deep-sea in situ observations.

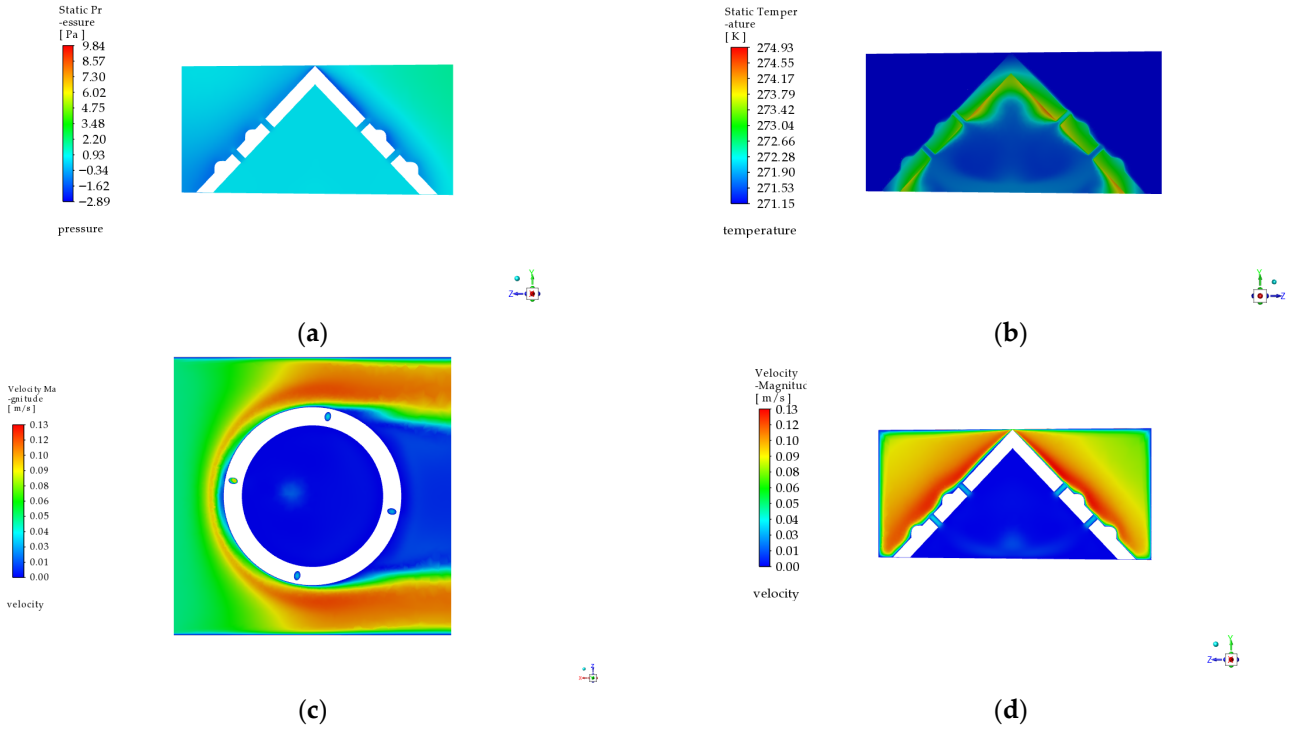

Figure 12. Cross-sectional contours of the internal and external fluid fields for the proposed probe design (2.0 mm aperture) in a simulated sulfide borehole environment. (**a**) Static pressure distribution at the YZ interface. (**b**) Static temperature distribution at the YZ interface. (**c**) XZ interface speed size release. (**d**) YZ interface speed size release.

Compared with traditional seafloor observation instruments such as node-based seismometers, chained seismographs, and seafloor observation networks, the proposed in situ observation probe features a more compact structure, high integration, and an

optimized conical bottom-end design that allows autonomous penetration into seafloor sediments. This structural advantage enables close physical coupling with the seabed, facilitating high-fidelity, three-dimensional observation of seismic activity, temperature, and pressure within confined boreholes.

However, given the complexity and extreme nature of the deep-sea environment, the current system and experimental validations possess certain limitations that will guide our future work:

(1) Power Management Limitations: While the probe carries a built-in battery, its long-term, high-frequency data observation still requires a physical electrical connection to a seafloor base station to supply sustained power. To address this limitation, future research will focus on further enhancing the probe's low-power operational capabilities and implementing intelligent, event-triggered sampling strategies to significantly reduce energy consumption during periods without dynamic vibrations.

(2) Calibration and Vibration Testing Limitations: Although the laboratory vibration tests successfully validated the structural integrity and basic dynamic response of the integrated MEMS sensors, the current accuracy verification lacks an independent benchmark system. The present dynamic calibration relied primarily on the shaker table's internal baseline. To rigorously quantify the dynamic sensing fidelity, future laboratory calibrations will incorporate a high-precision reference seismometer as a comparative benchmark to further verify and optimize the dynamic accuracy of the MEMS array.

(3) Sea Trial and Environmental Validation Limitations: The operational capability of the system was initially verified through a shallow-water sea trial (approximately 20 m depth). We objectively acknowledge that this coastal environment does not fully replicate the extreme hydrostatic pressure, elevated temperatures, and complex fluid dynamics characteristic of deep-sea hydrothermal zones. Consequently, this deployment served primarily as a critical preliminary validation phase to verify the electromechanical integration, watertight sealing, and mechanical viability of the free-fall penetration mechanism. To comprehensively evaluate the probe's structural endurance and high-precision thermodynamic sensing capabilities under authentic operational stresses, full-scale deep-sea deployments at active sulfide deposit boreholes are scheduled for our subsequent research phases.

(4) Dynamic Sensing Sensitivity Limitations: It must be objectively acknowledged that the highly integrated nature of the probe entails inherent trade-offs in dynamic sensitivity. With a noise threshold of 7 μg rms at 1 Hz, the integrated MEMS accelerometer possesses significantly lower sensitivity compared to traditional broadband ocean bottom seismographs (OBS). Consequently, the proposed device cannot fully replace standard seafloor seismographs for the detection of weak, far-field microearthquakes. Rather, its application is highly specialized: the proposed probe is specifically designed for near-field observations of localized, higher-amplitude vibrations and structural tilts directly within the confined boreholes of marine hydrothermal vent zones.

6. Conclusions

In this study, a novel, highly integrated in situ observation probe was developed and systematically evaluated to address the critical need for long-term, multi-parameter monitoring within seafloor sulfide deposit boreholes. Through a combination of rigorous computational fluid dynamics (CFD) simulations, laboratory calibrations, and preliminary sea trials, the system's performance and reliability were comprehensively verified.

To optimize the physical coupling with confined seafloor sediments at target depths of up to 4000 m, an optimal 2.0 mm micro-aperture array was engineered at the conical

probe tip. High-fidelity thermal-fluid-solid coupling simulations demonstrated that under extreme deep-sea conditions (75 MPa hydrostatic pressure and 271.15 K ambient temperature), this structural design acts as an effective hydrodynamic damper. It successfully eliminates pressure signal attenuation across the housing and facilitates sufficient convective fluid exchange to neutralize internal electronic heat. Consequently, the design effectively mitigates thermal pollution and ensures the high-fidelity capture of authentic environmental thermodynamic data.

Furthermore, laboratory experiments and preliminary sea trials confirmed the system's electromechanical stability and high-speed dynamic data acquisition capabilities. Operating at a sampling rate of 200 Hz, the integrated MEMS sensor array achieved a high signal-to-noise ratio and a low root-mean-square error, proving its capability to accurately capture dynamic vibrations and geological events. Ultimately, the robust and modular structural design of the proposed device offers applicability for specific observations of marine hydrothermal vent areas; by simply replacing the internal sensing elements, the probe can be readily adapted to monitor a diverse array of oceanographic and geochemical parameters in extreme marine environments.

Author Contributions: H.D. was responsible for the design, simulation, calculation, and experimental aspects of the project; J.Z. was responsible for the planning and advancement of the project; X.G. participated in the research on mechanical and temperature/pressure sensors; C.T. participated in the advancement of the project; and B.S. provided experimental facilities and support. All authors have read and agreed to the published version of the manuscript.

Funding: This research was supported in part by National Natural Science Foundation of China (Grant No. 42127807). It was also funded by the Zhejiang Provincial Department of Education, Project Y202354010 and National Key Research and Development Project of China (2023YFC2811105).

Data Availability Statement: The data presented in this study are available on request from the corresponding author. The data are not publicly available due to institutional restrictions and the sensitive nature of the seafloor observation sites.

Conflicts of Interest: Author Bin Sui was employed by the company Hangzhou Hanlu Geophysical Exploration Co., Ltd. The remaining authors declare that the research was conducted in the absence of any commercial or financial relationships that could be construed as a potential conflict of interest.

References

1. Elderfiled, H.; Schultz, A. Mid-Ocean Ridge Hydrothermal Fluxes and the Chemical Composition of the Ocean. *Annu. Rev. Earth Planet. Sci.* **1996**, *24*, 191–224. [CrossRef]
2. Hannington, M.; Jamieson, J.; Monecke, T.; Petersen, S. Modern Sea-floor massive sulfides and base metal resources: Toward an estimate of global sea-floor massive sulfide potential. *Soc. Econ. Geol.* **2010**, *15*, 317–338.
3. Rona, P.A. Resources of the Sea Floor. *Science* **2003**, *299*, 673–674. [CrossRef]
4. Hannington, M.; Jamieson, J.; Monecke, T.; Petersen, S.; Beaulieu, S. The abundance of seafloor massive sulfide deposits. *Geology* **2011**, *39*, 1155–1158. [CrossRef]
5. Bramley, B.J.; Lehrmann, B.; Dutrieux, A.M.; Martins, S.; Iglesia, A.G.D.L.; Stobbs, I.J.; Barriga, F.J.A.S.; Bialas, J.; Dannowski, A.; Varady, M.E.; et al. Geological fate of seafloor massive sulphides at the TAG hydrothermal field (Mid-Atlantic Ridge). *Ore Geol. Rev.* **2019**, *107*, 903–925. [CrossRef]
6. Wang, Y.; Chen, J.W.; Guo, J.; Wang, W.; Fang, Y.P.; Ren, X.Y.; Zhou, P. Design and study of a deep-sea multi-depth in-situ pore water pressure-retaining sampler. *Mar. Georesources Geotechnol.* **2023**, *41*, 1370–1378. [CrossRef]
7. Patanker, S.V.; Spalding, D.B. A calculation procedure for heat. mass and momentum transfer in three-dimensional parabolic flows. *Int. J. Heat Mass Transf.* **1972**, *15*, 1787–1806. [CrossRef]
8. Chadwick, W.; Butterfield, D.; Embley, R.W.; Tunnicliffe, V. Spotlight 1: Axial Seamount. *Oceanography* **2010**, *23*, 38–39. [CrossRef]
9. Davis, E.E.; Sun, T.; Heesemann, M.; Villinger, H.; Wang, K. Deep-Sea Borehole Fluid Pressure and Temperature Observations at Subduction Zones and their Geodynamic Implications. *Can. J. Earth Sci.* **2024**, *62*, 684–709. [CrossRef]

10. Falkenberg, J.J.; Keith, M.; Haase, K.M.; Bach, W.; Klemd, R.; Strauss, H.; Yeo, I.A.; Rubin, K.H.; Storch, B.; Anderson, M.O. Effects of fluid boiling on Au and volatile element enrichment in submarine arc-related hydrothermal systems. *Geochim. Cosmochim. Acta* **2021**, *307*, 105–132. [CrossRef]
11. Kopf, A.; Freudenthal, T.; Ratmeyer, V.; Bergenthal, M.; Lange, M.; Fleischmann, T.; Hammerschmidt, S.; Seiter, C.; Wefer, G. Simple, affordable, and sustainable borehole observatories for complex monitoring objectives. *Geosci. Instrum. Methods Data Syst.* **2015**, *4*, 99–109. [CrossRef]
12. Wilcock, W.S.D.; Dziak, R.P.; Tolstoy, M.; Chadwick, W.W.; Nooner, S.L.; Bohnenstiehl, D.R.; Caplan-Auerbach, J.; Waldhauser, F.; Arnulf, A.F.; Baillard, C.; et al. The Recent Volcanic History of Axial Seamount: Geophysical Insights into Past Eruption Dynamics with an Eye Toward Enhanced Observations of Future Eruptions. *Oceanography* **2018**, *31*, 114–123. [CrossRef]
13. Yang, W.F.; Tao, C.H.; Liao, S.L.; Zhang, H.C.; Zhu, C.W.; Li, W.; Zhang, G.Y.; Wang, X.F.; Wang, L.S. Evolution of a seafloor massive sulfide deposit on axial volcanic ridges: A case study of the Duanqiao hydrothermal field, Southwest Indian Ridge. *Orig. Res.* **2025**, *11*, 1538022. [CrossRef]
14. Tao, C.H.; Guo, Z.K.; Liang, J.; Yang, W.F.; Liao, S.L.; Chen, M.; Zhou, F.; Chen, J.; Wang, N.N.; Liu, X.H.; et al. Sulfide metallogenic model for the ultraslow-spreading Southwest Indian Ridge. *Sci. China Earth Sci.* **2023**, *66*, 1212–1230. [CrossRef]
15. Yu, J.H.; Niu, X.W.; Jin, Z.D.; Niu, L.H.; Ruan, A.G.; Ding, W.W.; Zhu, X.Y.; Liu, Z.J.; Liu, B.W.; Zhuang, C.T.; et al. The seismometer-detached ocean bottom seismograph and its experiments in the Gakkel Ridge, Arctic Ocean. *Acta Seismol. Sin.* **2025**, *47*, 535–555.
16. Sutton, G.H.; Duennebier, F.K.; Watake, B.L. Coupling of ocean bottom seismometers to soft bottom. *Mar. Geophys. Res.* **1981**, *5*, 35–51. [CrossRef]
17. Liu, H.F.; Luo, Z.C.; Hu, Z.K.; Yang, S.Q.; Tu, L.C.; Zhou, Z.B.; Krakt, M. A review of high-performance MEMS sensors for resource exploration and geophysical applications. *Pet. Sci.* **2022**, *19*, 2632–2648. [CrossRef]
18. Xiao, D.W.; Zhu, Q.; Zhang, J.Z.; Xie, T.T.; Ji, Q. The Design and Data Analysis of an Underwater Seismic Wave System. *Sensors* **2025**, *25*, 4155. [CrossRef]
19. Bao, Y.J.; Liu, X.Y.; Ma, Y.X.; Sun, J.R.; Wang, J.L.; Gong, Y.J. A simulation of thermal coupling characteristics on deep-sea residual oil recovery via pipeline using thermophysical properties. *Sci. Rep.* **2025**, *15*, 38210. [CrossRef]
20. Wu, G.; Zhao, X.; Shi, D.; Wu, X. Analysis of Fluid–Structure Coupling Vibration Mechanism for Subsea Tree Pipeline Combined with Fluent and Ansys Workbench. *Water* **2021**, *13*, 955. [CrossRef]
21. Menter, F.R. Two-equation eddy-viscosity turbulence models for engineering applications. *AIAA J.* **1994**, *32*, 1598–1605. [CrossRef]
22. Bakica, A.; Malenica, Š.; Vladimir, N. Hydro-structure coupling of CFD and FEM-Quasi-static approach. *Ocean Eng.* **2020**, *217*, 108118. [CrossRef]
23. Barth, T.; Jespersen, D. The design and application of upwind schemes on unstructured meshes. In Proceedings of the Aiaa Aerospace Sciences Meeting, Reno, NV, USA, 9–12 January 1989.
24. Kenneth, G.; Connell, M.; Varoto, P.S. *Vibration Testing: Theory and Practice*, 2nd ed.; Wiley: New York, NY, USA, 2008.
25. Julius, B.; Piersol, A. *Random Data: Analysis and Measurement Procedures*, 4th ed.; Wiley: New York, NY, USA, 2010.

Disclaimer/Publisher's Note: The statements, opinions and data contained in all publications are solely those of the individual author(s) and contributor(s) and not of MDPI and/or the editor(s). MDPI and/or the editor(s) disclaim responsibility for any injury to people or property resulting from any ideas, methods, instructions or products referred to in the content.